

Origin of the yield stress anomaly in L1₂ intermetallics unveiled with physically-informed machine-learning potentials

Xiang Xu^{1,2,*}, Xi Zhang^{1,*}, Erik Bitzek³, Siegfried Schmauder², and Blazej Grabowski¹

¹*Institute for Materials Science, University of Stuttgart, Pfaffenwaldring 55, 70569 Stuttgart, Germany*

²*Institute for Materials Testing, Materials Science and Strength of Materials, University of Stuttgart, Pfaffenwaldring 32, 70569 Stuttgart, Germany*

³*Computational Materials Design, Max Planck Institute for Sustainable Materials, Max-Planck-Straße 1, 40237 Düsseldorf, Germany.*

*Emails: xiang.xu@imw.uni-stuttgart.de; xi.zhang@imw.uni-stuttgart.de

Abstract

The yield stress anomaly of L1₂ intermetallics such as Ni₃Al or Ni₃Ga is controlled by the so-called Kear-Wilsdorf lock (KWL), of which the formation and unlocking are governed by dislocation cross-slip. Despite the importance of L1₂ intermetallics for strengthening Ni-based superalloys, microscopic understanding of the KWL is limited. Here, molecular dynamics simulations are conducted by employing a dedicated machine-learning interatomic potential derived via physically-informed active-learning. The potential facilitates modelling of the dislocation behavior in Ni₃Al with near *ab initio* accuracy. KWL formation and unlocking are observed and analyzed. The unlocking stress demonstrates a pronounced temperature dependence, contradicting the assumptions of existing analytical models. A phenomenological model is proposed to effectively describe the atomistic unlocking stresses and extrapolate them to the macroscopic scale. The model is general and applicable to other L1₂ intermetallics. The acquired knowledge of KWLs provides a deeper understanding on the origin of the yield stress anomaly.

Keywords: Yield stress anomaly; Dislocation cross-slip; L1₂ intermetallics; Molecular dynamics simulations; Machine-learning potentials.

1 Introduction

Ni-based superalloys are used for turbine blades because they withstand thermal mechanical loadings under high turbine-entry temperatures [1, 2]. Over several generations of these superalloys and corresponding thermal barrier coatings, the turbine-entry temperatures have increased by 700 K [3], significantly improving the thermodynamic efficiency of aircraft engines. The outstanding thermal resistance mainly originates from a high volume fraction of L1₂-ordered precipitates. In contrast to common structural materials, the yield stress of certain L1₂ intermetallics, e.g., Ni₃Al [4] or Ni₃Ga [5], increases with temperature, typically accompanied with an anomalously increasing work-hardening rate. As this so-called yield stress anomaly (YSA) is pivotal for strengthening advanced alloys, the steady increase of understanding YSA has been a key ingredient not only to the evolution of Ni-based superalloys [1, 2, 6] and Co-based superalloys [7–9], and also for the development of L1₂ strengthened high-entropy alloys [10, 11].

However, the origin of YSA is still not satisfactorily clarified [6]. What is known from transmission electron microscopy (TEM) on samples deformed in the temperature region of the YSA [12, 13] is that the dislocations in Ni₃Al exhibit a unique non-planar dislocation core structure—nowadays referred to as the Kear-Wilsdorf lock (KWL). The dislocation core was shown to evolve through cross-slip [14, 15] in which three planar defects are involved: two antiphase boundaries (APBs) on the (100) and (111) planes plus a complex stacking fault (CSF).

Several analytical models [16–22] have been proposed to comprehend KWLs and their relation to YSA, considering factors like the difference between the formation energies of the (111)APB and (100)APB [16],

and torque interactions between the superpartials [17]. The ‘‘APB-jump’’ phenomenon observed in *in situ* TEM experiments [14] brought forward a model based on the competition between the formation and unlocking of the incomplete KWL [19]. An incomplete KWL is built up from APBs on both the (100) and (111) planes while a complete KWL contains only an APB on the (100) plane (see Figure ?? in Supplementary Material). A common limitation of existing models is the assumption of an athermal unlocking process [19, 21].

Despite the importance of KWLs, the understanding of their formation and unlocking is limited, especially regarding the atomistic evolution during cross-slip. A close atomistic inspection is difficult with experiments, but becomes feasible with atomistic simulations. For example, the embedded atom method (EAM) has been used to investigate the dissociation of superdislocation in Ni₃Al [23, 24], to calculate the nucleation energy of the cross-slip process for a single dislocation [25, 26] and for intersecting dislocations [27]. These simulation studies focused on energetics at 0 K and thus neglected entropy contributions relevant at elevated temperatures. Recently, the temperature-dependent dislocation dynamics of edge dislocation in Ni₃Al has been investigated using EAM potential [28]. However, atomistic simulations for the behavior of screw superdislocations, particularly when related to KWLs and cross-slip processes at elevated temperatures, are still absent. This is presumably due to the limited accuracy of existing potentials in predicting the energetics of planar defects, which prevents the occurrence of dislocation cross-slip.

In the present study, a machine-learning interatomic potential (MLIP), specifically a Moment Tensor Potential (MTP) [29, 30], is developed and utilized to simulate the dislocation activity in Ni₃Al at near *ab initio* accuracy and with inclusion of finite temperature effects. The most critical aspect in designing MLIPs is the proper choice of the fitting dataset from density functional theory (DFT). To guarantee an accurate description of the dislocation, we utilize a physically-informed active-learning scheme and evaluate the MLIP specifically on the temperature dependence of the planar defect energies. The MLIP enables the study of the unlocking of KWLs by shearing at different temperatures in molecular dynamics (MD) simulations. Based on the obtained data, a phenomenological model for *thermally* activated KWL unlocking is derived.

2 Results

2.1 Physically-Informed Active Learning

Active-learning (AL) [30] has been successfully used in different machine-learning studies [31, 32]. However, for the present purpose, the standard AL scheme cannot be applied due to the large, DFT-inaccessible supercell size required to model a KWL (> 1 million of atoms). Hence, we devise a modified AL scheme, in the spirit of two very recent schemes applied to large-scale silicon-oxygen systems [33] and to dissociated partial dislocations [34]. The key idea is to decompose the KWL into its physically relevant parts which *can* be modelled with (periodic) DFT. The choice of the relevant parts is guided by domain expertise and is displayed in Figure 1(a). Besides the perfect bulk, which is clearly required as the basic fitting input, we know that a KWL is formed by the (100)APB, the (111)APB, and the CSF. For the present shearing simulations, we also need the (111) surface due to the boundary conditions. Additionally, we include the superlattice intrinsic stacking fault (SISF), and Al and Ni vacancies into the fitting dataset for a broader applicability of the MLIP, for example for investigations of creep properties.

For each such geometry a usual AL is performed at a high temperature (here 1600 K). The different AL steps are executed successively in a row. We start with the perfect bulk AL and take the resulting MTP as input to the next AL step for the (100)APB. This process continues for the remaining geometries until a final MTP is obtained. The sequence is displayed in Figure 1(a). Fitting the MTP in such a systematic way allows us to monitor the accuracy at each step. As usual, one measure of the MTP accuracy is the root mean square error (RMSE) in energies and forces. The force RMSE stays almost unchanged while the energy RMSE increases by a factor of 2.4 during the AL steps (cf. Figure 1(a)). The final training errors of 1.59 meV/atom and 0.056 eV/Å are small considering the high temperature and structural complexity of the fitting dataset.

An additional measure that we employ here and that gives us control over the accuracy in describing the geometry of interest, i.e., the KWL, is the locally resolved extrapolation grade. The extrapolation

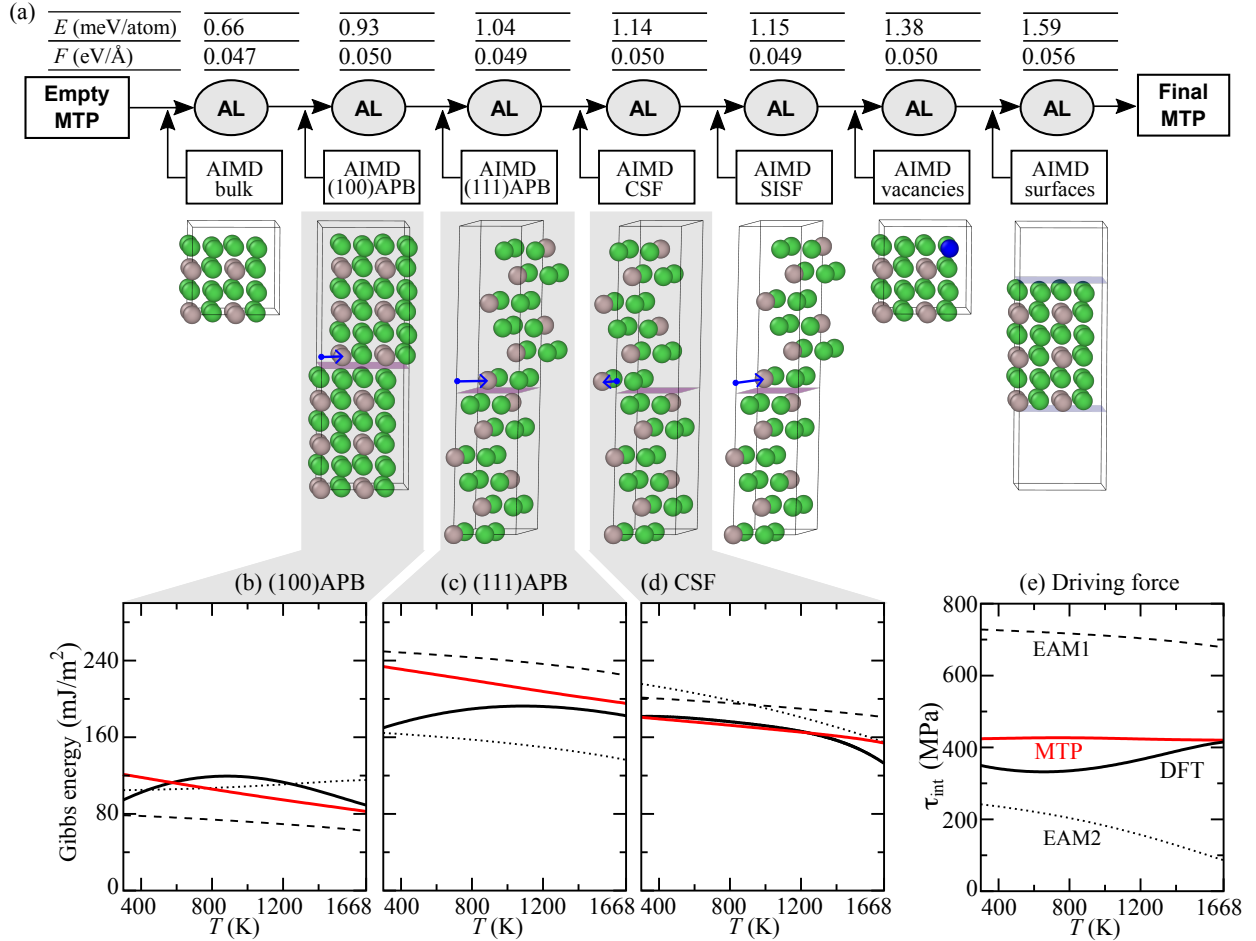


Figure 1: Machine-learning potential design. (a) Flow-diagram of the proposed physically-informed active-learning scheme. Every oval labelled “AL” represents a standard active-learning step for the indicated geometry, i.e., bulk structure, (100)APB, (111)APB, CSF, superlattice intrinsic stacking fault (SISF), Ni-vacancy, Al-vacancy, and a surface with its normal along the [100] direction. The atomic structures are simplified for a better illustration. The blue arrows indicate the vectors of the relative shifts needed to generate the planar defects. The input for each subsequent AL-oval is 1) the MTP from the previous AL-step and 2) a set of AIMD configurations for the new geometry to provide basic structural information. The root mean square errors (RMSEs) above each oval represent the fitting errors when completing the respective AL-step. (b) - (d) Temperature-dependent Gibbs formation energies of the planar defects predicted by the *final* MTP. (e) Driving force for the cross-slip process originating from the difference of the two APB energies in combination with the anisotropic factor (cf. Equation (??) and the related discussion in Supplementary Material). DFT results are from previous works [35, 36]. Dashed (EAM1) and dotted (EAM2) curves show results from the EAM potentials modified by Mishin *et al.* [37] and Du *et al.* [38], respectively.

grade is a metric that quantifies how far away a certain atomic configuration is located in phase space with respect to the fitting dataset.¹ The advantage is that no extra DFT calculation is required and thus the grade can be computed for the target geometry even if a large supercell is required, as for the KWL. Specifically, we utilize our final MTP to generate KWL snapshots for which we resolve the extrapolation grade locally. We do this for the different MTPs obtained from our physically-informed AL scheme and investigate how the grade changes along the sequence of AL steps (Supplement Figure ??). The MTP trained with bulk structures only (MTP-bulk) describes the perfect bulk atoms (i.e., 98.8% of all

¹Numerically, extrapolation by the MTP occurs if the grade is greater than unity. The higher the extrapolation grade the severer is the extrapolation by the MTP.

atoms) with a grade of $\lesssim 1$ which indicates an interpolative behavior. Atoms belonging to the KWL are revealed to have a slightly higher grade which indicates an extrapolative behavior. Upon inclusion of the (100)APB and (111)APB geometries into the physically-informed AL, the extrapolation grade steadily improves, reaching a grade of $\lesssim 1$ also in the KWL region. The analysis of the local grade thus gives increased confidence in the predictive capability of the MTP in the most relevant simulation region.

As a further quality measure, the final MTP is evaluated on the free energy surfaces for bulk Ni_3Al , the APBs, and the CSF, up to the melting point 1668 K. The thermal properties of perfect bulk Ni_3Al are well predicted by the MTP over a large temperature range (Figure ?? in the Supplementary Material). The resulting temperature-dependent planar defect energies (red curves in Figure 1 from (b)-(d)) are likewise in good agreement with the explicit DFT results (black curves) [35,36], in particular in the most relevant temperature range for the KWL simulations around 1000 K. Of special importance is the fact that the internal driving force to form a KWL (Figure 1(e)), which originates from the difference of the two APB energies in combination with the anisotropic factor (cf. Equation (??)) and which the two available EAM potentials strongly under- or overestimate, is close to DFT for the MTP.

2.2 Formation of KWL

With the optimized MTP, the KWL can be readily created. Figure 2 documents the formation of an incomplete KWL as observed in an MD simulation at 980 K (without external loading). The corresponding dislocation core configurations are detailed in Section ?? in the Supplementary Materials. In additional test simulations with EAM potentials [37,38], such a spontaneous KWL formation is not observed at similar temperatures.²

Snapshots (a) to (c) illustrate the first cross-slip process required to form a KWL. In snapshot (a), the dislocation is initially fully dissociated on the (111) plane, with each superpartial split into a pair of Shockley partials separated by a CSF ribbon. Then, the lower superpartial cross-slips from the (111) plane to the ($\bar{1}\bar{1}1$) plane, partially in (b) and fully in (c). At 1234 ps, the second cross-slip of the lower superpartial, from the ($\bar{1}\bar{1}1$) plane to another (111) plane, is initiated (Figure 2(d)). When this double cross-slip process is finished, an incomplete KWL has formed (Figure 2(f)).

It is worth noting that the distance between the original (111) plane and the (111) plane onto which the superpartial moves during the second cross-slip process is 2δ (see the side view in Figure 2(d) and (e) and the enlarged front view in Figure 2(g)), where δ labels the distance between the two nearest atomic planes along the [111] direction. Our results are in agreement with a recent *in situ* scanning tunnelling microscopy study [15] which reported 2δ at room temperature and $m\delta$ (with $m \geq 2$) at higher temperatures in Ni_3Al (1 at.% Ta), however, without an interpretation. It is the strong internal forces that drive the CSF ribbon in the lower superpartial away from the original (111) plane. An internal torque due to the anisotropic elastic interaction between the two screw superpartials [17,40], indicated in the side view of Figure 2(b) by the gray arrows, pushes the upper superpartial to the left and the lower superpartial to the right (note that the Burgers vector points out of the paper plane). In the analyzed simulation, the lower superpartial cross-slips first. (The leading and trailing superpartials have the same probability to cross-slip onto a (100) plane, as indicated by Figure ?? in the Supplementary Materials.) When it is located on the ($\bar{1}\bar{1}1$) plane, the repulsive force between the two superpartials (cf. double headed arrow in the side view in Figure 2(d)) drives the lower superpartial to cross-slip again, now to the (111) plane which is 2δ away from the original one. The observed atomistic shape of the cross-slipped segment, specifically the well-defined 2δ distance over the full segment shown in Figure 2(g), supports the previously suggested “double-jog” mechanism [18]. MD observations show that the jogs are highly mobile and expand rapidly along the dislocation line. Incomplete KWLs with 3δ or 4δ likewise occur in the MD simulations. They form by consecutive cross-slips of both of the superpartials.

The present MD simulations reveal the importance of the superpartial splitting and of the corresponding CSF on the cross-slip behavior. This is a crucial insight, since available phenomenological models [16,18,19] do not explicitly take into account the screw superpartial splitting into Shockley partials. This approximation of considering only *constricted* superpartials favors 1δ -KWL formation at low temperatures and renders 1δ -KWLs to be the intermediate state for forming $m\delta$ -KWLs at elevated

²Our calculations show that for the Mishin-EAM [37] a KWL forms for an overheated system at 1200 K and that no KWL formation is feasible for the Du-EAM [38] within the typical MD time scale.

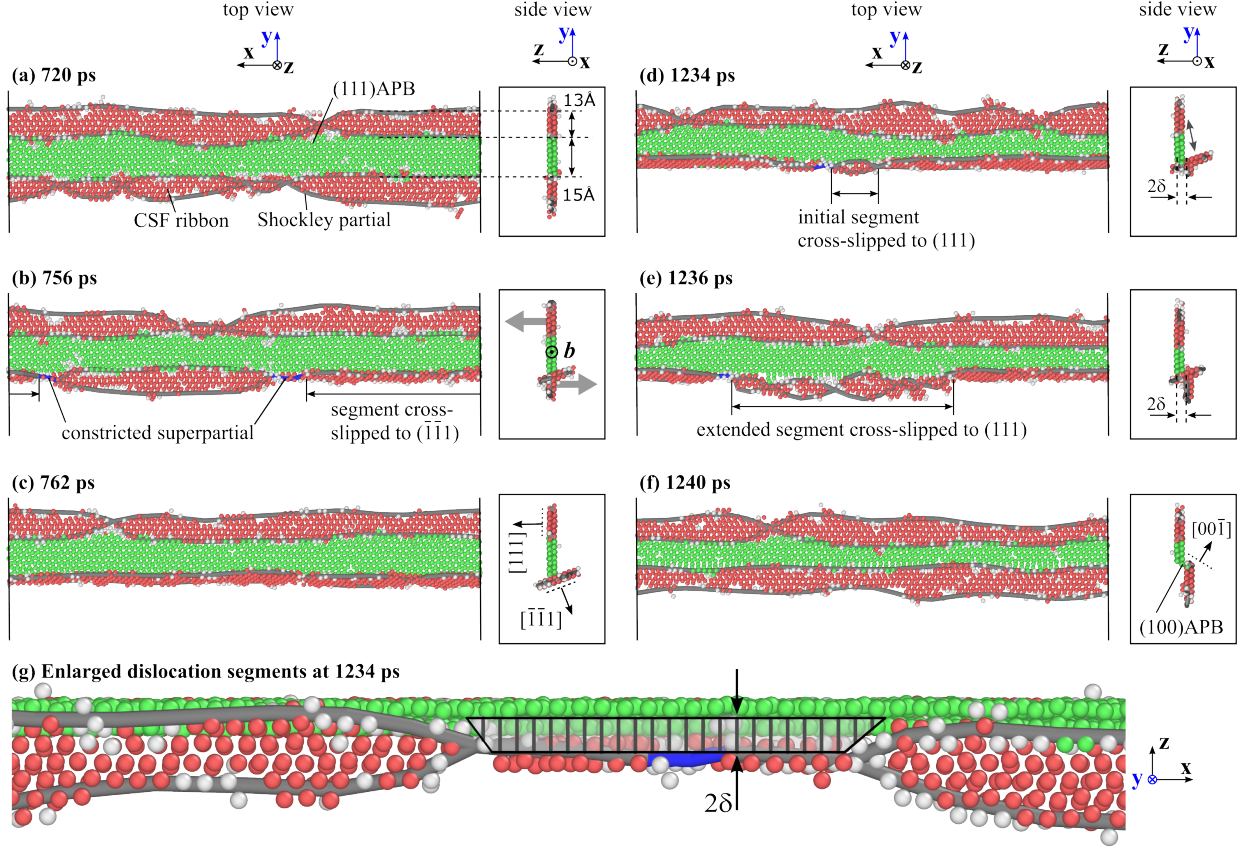


Figure 2: Formation of an incomplete KWL at 980 K. Snapshots (a) to (c) display the first cross-slip from a (111) to a $(\bar{1}\bar{1}1)$ plane, and snapshots (d) to (f) the second cross-slip from the $(\bar{1}\bar{1}1)$ plane to another (111) plane. (g) Enlarged dislocation segments at 1234 ps. The dislocation structure is analyzed by using the Dislocation Extraction Algorithm (DXA) in Ovito [39]. Green and red atoms highlight the APB region and the CSF ribbon, respectively. For a clear illustration, atoms not related to the dislocation core structure are removed. The gray tubes highlight Shockley partials and the blue ones constricted superpartials.

temperatures. In contrast, the MD simulations show that a 2δ -KWL can form directly without an intermediate 1δ -KWL. We conclude that this is due to the CSF ribbon spanning on the $(\bar{1}\bar{1}1)$ plane. This finding highlights the necessity to carefully consider the effect of the superpartial splitting into Shockley partials and the CSF ribbon on the dislocation behavior.

2.3 Unlocking of KWL

The above-discussed KWL with the cross-slip distance of 2δ was sheared at different temperatures T and shear rates $\dot{\gamma}$. The unlocking of the KWL at temperatures $\lesssim 1000$ K involves a two-step cross-slip process, in reverse order compared to its formation. Figure 3 shows a representative stress-strain curve in (a) and selected dislocation structures at critical simulation times in (b).

The shear stress increases with strain at a slope of 45 GPa until point (III) when full unlocking occurs. At the earlier point (II), the trailing superpartial cross-slips from its nesting (111) plane to the $(\bar{1}\bar{1}1)$ plane (difference between the configurations in (I) and (II) in Figure 3(b)) accompanied by a small stress drop. The second cross-slip of the trailing superpartial from the $(\bar{1}\bar{1}1)$ plane to the (111) glide plane, which hosts the leading superpartial and the APB, happens at point (III) and is followed by a rapid glide of the dislocation (cf. perspective view (IV) in Figure 3(b)). Accordingly, a stress collapse is observed in the stress-strain curve. After unlocking, the released dislocation either glides freely on the (111) plane or cross-slips to a (100) plane forming a KWL again. The latter occurs in particular at higher temperatures.

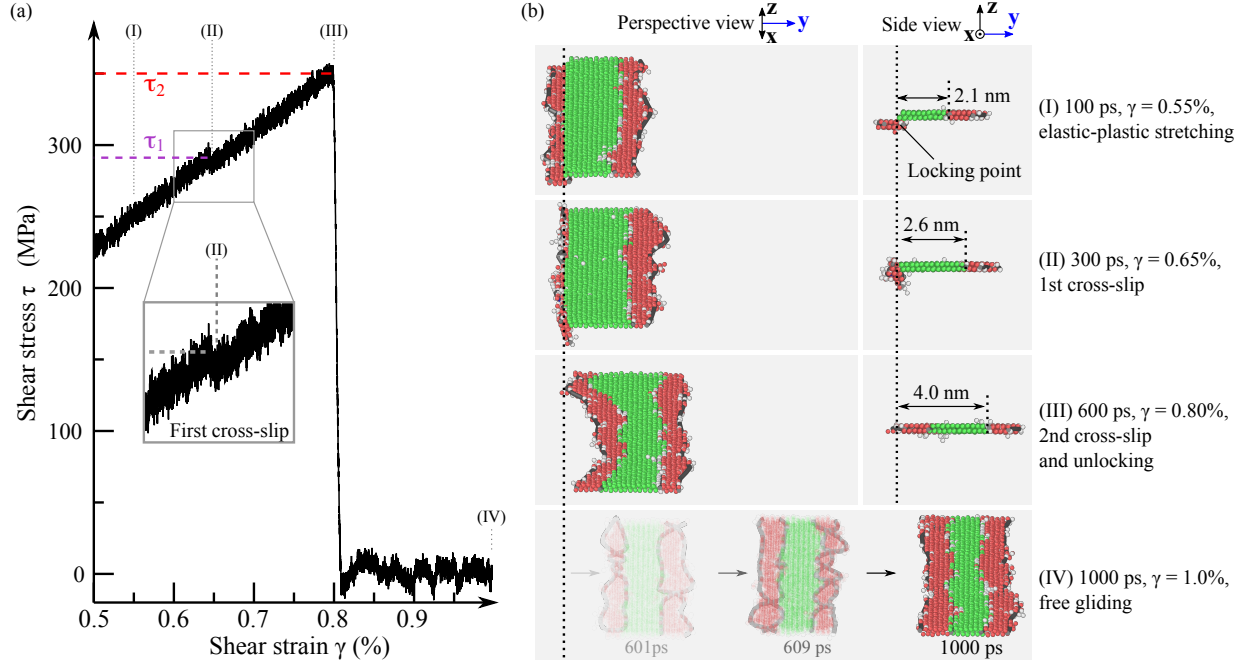


Figure 3: Unlocking of a KWL at $T = 1000$ K and $\dot{\gamma} = 5 \times 10^{-6}$ ps $^{-1}$. (a) Corresponding stress-strain curve and (b) snapshots at representative times highlighting the evolution of the KWL during unlocking. Snapshot (IV) has only a perspective view. The given times are referenced with respect to the time at the shear strain of $\gamma = 0.5\%$. Atom colors have the same meaning as in Figure 2. The moving direction, i.e., the y -axis, is colored in blue.

An exemplary run at a slightly higher temperature of 1050 K is shown in Figure 4. Many cross-slip events occur during this simulation and various distinct core configurations of the superdislocation are observed. In addition to the 2δ configuration found for the KWL-formation and unlocking simulation at lower temperatures, here, core configurations can also exist with larger δ values for the superpartials separation, e.g., 3δ (snapshot at 320 ps), 4δ (1580 ps), 5δ (1820 ps), or 6δ (1980 ps). In contrast to the initial KWL-formation, the double cross-slip events at larger separations occur in steps of 1δ , which is a consequence of a smaller driving force. Some of the cross-slip events can be correlated with previous TEM observations [14].

The “APB-jump” observed in *in situ* TEM experiments [14] is replicated on the atomic scale at a shear strain of 1.05%, as illustrated in Figure 4 in the box labelled “APB-jump”. This kind of jump starts from a core structure with two (111)APBs lying connected on two neighboring (111) planes. During the APB-jump, the trailing superpartial cross-slips from the $(\bar{1}\bar{1}1)$ to the lower (111) plane and glides on this (111) plane by a short distance (2.7 nm), which reflects the (111)APB width corresponding to the instantaneous loading state, before cross-slipping to another $(\bar{1}\bar{1}1)$ plane.

Another kind of jump (labelled “dislocation-jump”) happens at a slightly higher strain of 1.17%, during which the released dislocation moves shortly freely on the (111) plane but quickly gets stopped due to a cross-slip event. This “dislocation-jump” is, from a broader perspective, similar to the previously observed “long distance jump” [14] but different in the details of the mechanism proposed in that work. From the MD snapshot at 1400 ps, it is the trailing superpartial that firstly cross-slips to another $\{111\}$ plane rather than the leading one. A more detailed analysis of the MD simulations shows the mechanism of this “dislocation-jump” to be an inertia effect which asymmetrically impacts the motion of the leading and trailing superpartials. The consequence are asymmetric elastic vibrations of the core structure on the slip plane, different velocities of the leading and trailing superpartial, and eventually different cross-slip rates. We speculate that this dislocation jump is related to the jerky movement of dislocations in L1₂ intermetallics and suggest further research in this direction.

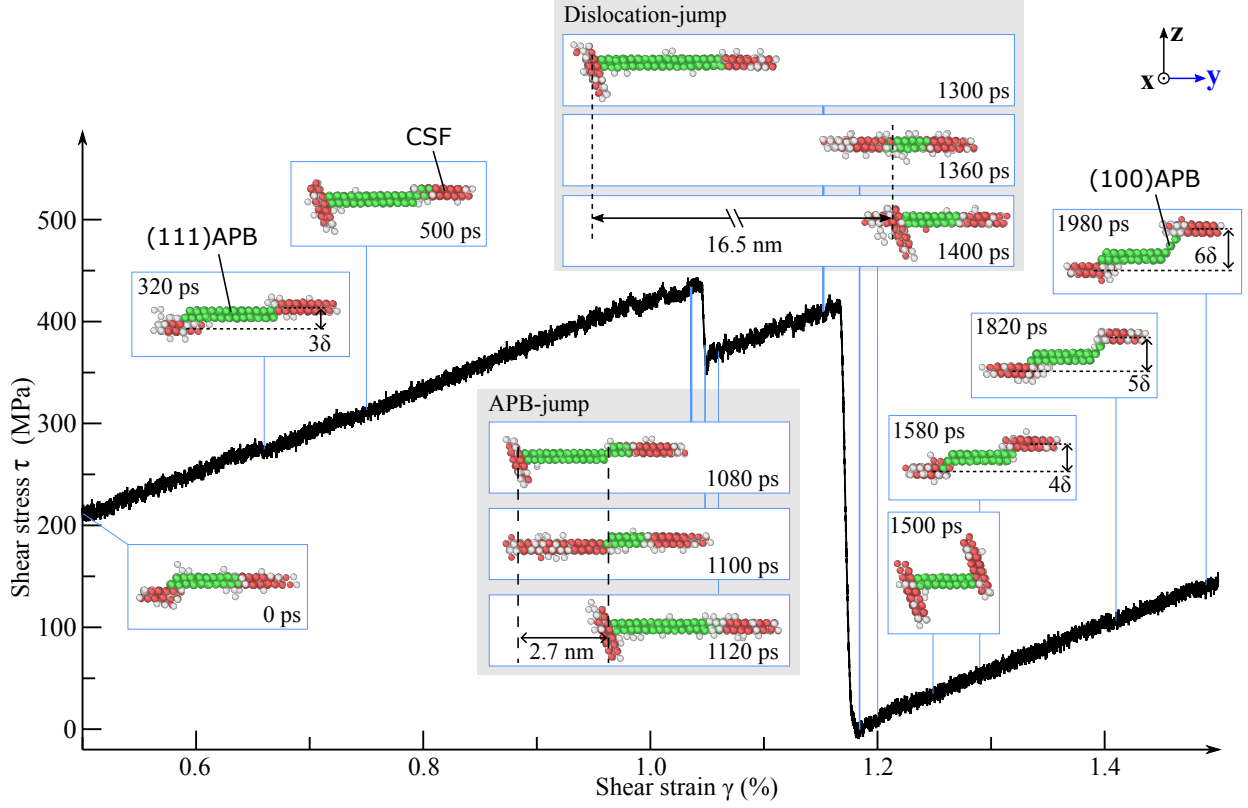


Figure 4: Unlocking of a KWL at $T = 1050$ K and $\dot{\gamma} = 5 \times 10^{-6}$ ps $^{-1}$. The given times are referenced with respect to the time at $\gamma = 0.5\%$. Atom colors have the same meaning as in Figure 2.

2.4 Temperature-dependent critical Stresses

Figure 5 shows the temperature-dependence of the stresses required to unlock a KWL. The lower stress τ_1 corresponds to the first cross-slip of the trailing superpartial. The higher stress τ_2 reflects the highest stress required to unlock the KWL, which can correspond for example to the second cross-slip of the trailing superpartial or a dislocation jump (cf. discussion in Sec. 2.3). For both stresses, a strong decrease with temperature is observed. In particular, the unlocking stress τ_2 significantly drops by almost 40% from 568 MPa at 650 K to 351 MPa at 1000 K, suggesting that in the temperature region of YSA, the unlocking of KWLs has a substantial thermal contribution.

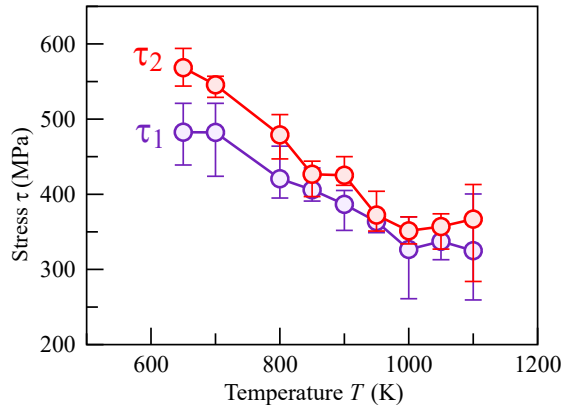


Figure 5: Temperature-dependent critical stresses at a shear rate of $\dot{\gamma} = 2 \times 10^{-6}$ ps $^{-1}$. Error bars are determined from three statistical samples.

Above 1000 K, the two critical stresses exhibit significant statistical fluctuations. Within the

available statistics, the averaged τ_1 remains almost unchanged, whereas the unlocking stress τ_2 increases slightly with temperature. The latter is due to the increased cross-slip distances at high temperatures (cf. Figure 4). In this temperature region, the weak temperature dependence indicates that the thermal component required to constrict the Shockley partials is rather small and the unlocking process depends mainly on the internal elastic interactions between two superpartials, i.e., the athermal component.

2.5 Phenomenological Model

With the atomistically obtained temperature-dependent unlocking stresses, we derive a phenomenological model to predict the unlocking of KWLs, the essence of which is schematically depicted in Figure 6(a). We decompose the effective stress τ_{eff} required to unlock a KWL into a static component τ_{st} that balances the internal interaction and a thermal component τ^* required to overcome the barrier of the thermally-activated unlocking,

$$\tau_{\text{eff}}(T) = \tau_{\text{st}}(T) + \tau^*(T) = \underbrace{\tau_{\text{at}} - \tau_{\text{soft}}(T)}_{\text{static } \tau_{\text{st}}} + \tau^*(T), \quad (1)$$

where, as indicated, τ_{st} is further decomposed into an athermal term τ_{at} and a softening term τ_{soft} . The thermal softening term τ_{soft} accounts for, e.g., the reduced elastic constants at elevated temperatures. The frictional force is implicitly taken into account by fitting to the unlocking stresses.

For a thermally-activated process, the energy barrier ΔH can be expressed as [32, 41–43]

$$\Delta H = H_0 \left[1 - \left(\frac{\tau^*}{\tau_{0\text{K}}^*} \right)^p \right]^q, \quad (2)$$

where H_0 is the enthalpy when τ^* is zero and $\tau_{0\text{K}}^*$ is the stress to overcome the barrier at 0 K; p and q are activation exponents, for which $p = 0.5$ is widely used for dislocations [21, 42, 43] and $q = 3/2$ is considered to be general for thermally-activated processes [21, 44].

The energy barrier ΔH is related to the strain rate $\dot{\gamma}$ via [42, 43]

$$\frac{\dot{\gamma}}{\dot{\gamma}_0} = \exp \left(-\frac{\Delta H}{k_{\text{B}}T} \right), \quad (3)$$

with $\dot{\gamma}_0$ a pre-factor and k_{B} the Boltzmann constant. Combining Equations (2) and (3), the thermal part τ^* can be written as:

$$\tau^*(T) = \tau_{0\text{K}}^* \left[1 - \left(-\frac{k_{\text{B}}T}{H_0} \ln \frac{\dot{\gamma}}{\dot{\gamma}_0} \right)^{2/3} \right]^2. \quad (4)$$

With increasing temperature, the term inside of the square brackets decreases from 1 at $T = 0\text{ K}$ to 0 at a temperature at which the process is fully activated and which we label T_1 . With the assumption of a linear temperature dependence of the thermal softening term, i.e., $\tau_{\text{soft}}(T) = \epsilon \cdot T$, the effective stress reads

$$\tau_{\text{eff}}(T) = \tau_{\text{at}} - \tau_{\text{soft}}(T) + \tau^*(T) = \tau_{\text{at}} - \epsilon \cdot T + \tau_{0\text{K}}^* \left[1 - \left(-\frac{k_{\text{B}}T}{H_0} \ln \frac{\dot{\gamma}}{\dot{\gamma}_0} \right)^{2/3} \right]^2, \quad (5)$$

with the thermal term $\tau^*(T)$ cut off at T_1 . We fit the unlocking stresses τ_2 obtained from MD simulations at different $\dot{\gamma}$ and T (up to 1000 K) with the derived phenomenological model (Equation (5)) and obtain the values given in Table 1. The resulting curves for the investigated strain rates are plotted in Figure 6(b). While the static term τ_{st} , shown as the dashed line labelled “static”, demonstrates a slight temperature dependence, the thermally-activated term $\tau^*(T)$ represented by the distance between the fitted curve and the “static” line rapidly increases with decreasing temperatures.

Table 1: Optimized fitting parameters for the phenomenological model in Equation (5).

τ_{a} (MPa)	$\tau_{0\text{K}}^*$ (MPa)	$\dot{\gamma}_0$ (ps ⁻¹)	H_0 (eV)	ϵ (MPa/K)
463.2	1661.2	4.88×10^{-2}	1.10	0.138

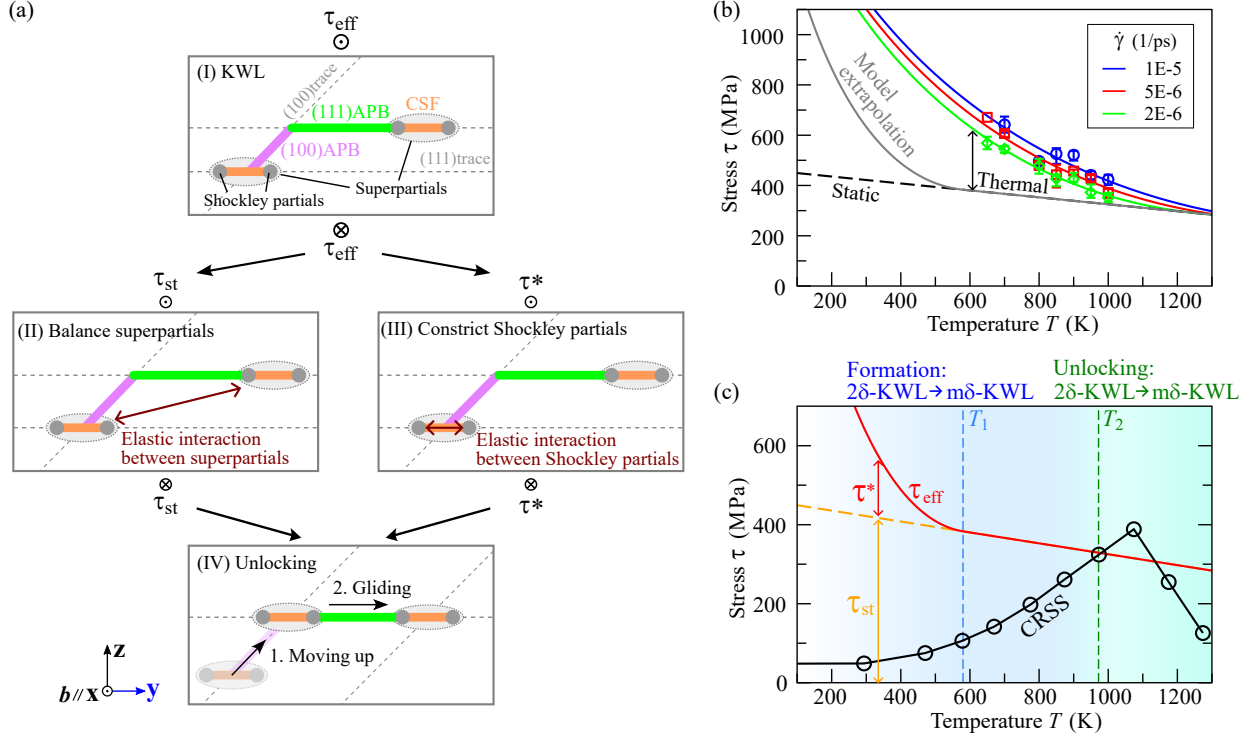


Figure 6: Phenomenological model describing the evolution of screw superdislocations in L1₂ intermetallics. (a) Schematic diagram for the decomposition of the effective stress to unlock a KWL. The applied shear stress points into (\otimes) or out of (\odot) the page. For simplicity, the lattice friction acting against dislocation movement is neglected in the illustration. (b) Effective stresses fitted to Equation (5) and the model extrapolation to the macroscale (gray curve). The colored symbols denote values from the MD simulations and the corresponding solid curves represent the model fit at the given shear rates. (c) Comparison between the macroscopic unlocking stress and the critical resolved shear stress (CRSS) (from the 0.2% proof stress) [4].

3 Discussion

The proposed model, derived from atomistic simulations, can be employed to predict the macroscopic unlocking stress and thereby to achieve a better understanding of the YSA. To this end, the macroscopic process is treated as a collection of microscopic unlocking events of single dislocations, each of which can be described by Equation (5) with the here obtained parameters (Table 1). This is reasonable because the YSA is known to be mainly caused by cross-slip events that lead to an exhaustion of single, mobile dislocations [15, 19, 21]. Therefore, the macroscopic unlocking stress can be obtained by substituting the logarithmic term in Equation (5) with its macroscale counterpart $\ln(\dot{\gamma}_m/\dot{\gamma}_{m,0})$, with $\dot{\gamma}_m$ and $\dot{\gamma}_{m,0}$ obtained from Ref. [4] and from Orowan's Equation, respectively (see Supplementary Material for details). The resulting temperature-dependent macroscopic unlocking stress is shown in Figure 6(b) (gray curve). The thermal part of the macroscopic unlocking stress is leftwards shifted, i.e., there is a smaller thermal contribution compared to the microscopic curves due to the longer accessible time frames on the macroscale.

The calculated temperature-dependent macroscopic unlocking stress sheds light on the interpretation of the YSA and the accompanying anomalous work-hardening rate, particularly when it is compared with the measured critical resolved shear stress (CRSS) at 0.2% plastic strain for Ni₃Al (black curve) [4], as plotted in Figure 6(c). Two critical temperatures, T_1 and T_2 , are relevant for the formation and the unlocking of KWLs.

Formation of KWLs. The thermally-activated component τ^* reduces with increasing temperature and becomes zero at T_1 . Along with the decrease of τ^* , the formation of KWLs driven by internal

interactions becomes easier due to a reduced cross-slip barrier (without external loading). Therefore, mobile dislocations have a rapidly increasing propensity to get exhausted, resulting in an increase of the dislocation exhaustion rate. This interpretation is in agreement with experimental studies [20, 45]. The CRSS and the work-hardening rate $\theta_{0.2}$ (θ at 0.2% plastic strain) increase with temperature. From T_1 onward, a Shockley pair bound by a CSF ribbon can easily constrict and, consequently, most screw dislocations transform into 2δ -KWLs due to the strong internal driving force. Since 2δ -KWLs with constricted superpartials are only metastable, the superpartials further cross-slip along the (100) plane to form $m\delta$ -KWLs with $m > 2$ or even complete KWLs, which require higher stresses to unlock. These types of KWLs have been frequently observed in TEM studies at elevated temperatures [46, 47]. The CRSS and the work-hardening rate $\theta_{0.2}$ increase with temperature at a faster rate.

Unlocking of KWLs. At T_2 , the CRSS reaches the stress required to unlock 2δ -KWLs as predicted by the proposed model. The unlocking of 2δ -KWLs suppresses the formation of $m\delta$ -KWLs with $m > 2$, thus reducing the exhaustion rate and the work hardening rate $\theta_{0.2}$. The work-hardening rate $\theta_{0.2}$ consequently reaches its maximum around T_2 . A similar conclusion was made in Ref. [48] where various experimental measurements were carefully analyzed and in Ref. [49] where the YSA of three L1₂ intermetallics with extreme values of planar-defect formation energies was compared. The here obtained $T_2 = 970$ K compares well with the experimentally measured value of 800-850 K at 0.2% plastic strain [45, 49]. Upon a further increase of the CRSS, $m\delta$ -KWLs with $m > 2$ can be unlocked, and at the critical, maximal value of the CRSS, other gliding mechanisms become active, e.g., gliding on the (100) plane [6] and the APB dragging mechanism [47].

The proposed phenomenological model does not only explain the macroscopic YSA of Ni₃Al via the evolution of KWLs, but also clarifies the role of the different planar defects on the YSA by the decomposition into a “static” and a “thermal” component (cf. Figure 6). The difference in the two types of APBs contributes mostly to the internal elastic interactions between the superpartials, determining the magnitude of the static component (cf. Equation (??)). The CSF energy controls the thermally-activated constriction of the Shockley partials. Note that the static component turns into the driving force during the formation of KWLs acting against the thermal constriction.

The above discussion and the proposed model can be transferred to understand the yield behavior of other L1₂ intermetallics, for example, Co-based intermetallics [8, 9] and L1₂ strengthened high-entropy alloys [10]. To apply the model, the system-specific model parameters have to be determined. For example, H_0 can be obtained based on the CSF energy and dislocation interactions [50, 51]; τ_{at} is given by the APB energies and the elastic anisotropic factor (cf. Equation (??)); ϵ can be evaluated from the temperature dependence of the elastic constants. With these parameters, T_1 and T_2 are readily available. In addition to regulating the formation of KWLs, T_1 is also an important factor for determining the activation of gliding systems on {100} planes, as previously pointed out for L1₂ intermetallics with high CSF energy [49]. In this respect, the proposed model facilitates the establishment of general constitutive laws for describing the yield behavior of L1₂ intermetallics. Tuning YSA for L1₂ intermetallics by tailoring the formation energy of planar defects *in silico* is a promising avenue, for example, with the assistance of high-throughput tools [52].

In conclusion, KWLs, the origin of YSA in L1₂ intermetallics, can be successfully formed and unlocked *in silico* at the atomistic scale by using an *ab initio*-based and physically-informed machine-learning potential. The simulations show a significant temperature dependence of the unlocking stresses, in contrast to previous athermal predictions. To describe the unlocking stresses, we have derived a phenomenological model that integrates both the athermal component and the thermally-activated component, and that can be extrapolated to the macroscopic scale. By comparing the extrapolated results with experimental values, two critical temperatures are identified, which are of crucial importance to predict the evolution of KWLs. The atomistic simulations predict many cross-slip events, some of which reenact experimental observations, such as the direct formation of 2δ -KWLs, the APB-jump, and the dislocation jump. The applicability of the here-acquired knowledge and the phenomenological model to other L1₂ intermetallics has been elaborated.

4 Methods

4.1 Moment Tensor Potential

The moment descriptor $M_{\mu,\nu}$ in the MTP formalism describes atomic interactions with both radial and angular information according to [29]

$$M_{\mu,\nu} = \sum_j f_\mu(|\vec{r}_{ij}|, z_i, z_j) \underbrace{\vec{r}_{ij} \otimes \cdots \otimes \vec{r}_{ij}}_{\nu \text{ times}}, \quad (6)$$

in which $f_\mu(|\vec{r}_{ij}|, z_i, z_j)$ is the radial function for particle i (type z_i at \vec{r}_i) interacting with its neighbor j (type z_j at \vec{r}_j); μ stands for the number of radial functions (depending on the level of the contraction introduced next); $\vec{r}_{ij} \otimes \cdots \otimes \vec{r}_{ij}$ is a tensor of rank ν representing the angular interaction (\otimes denotes the outer product). The scalar contractions of the moments $M_{\mu,\nu}$ give the basis functions B_α . With these basis functions, the local interatomic potential $V(\mathbf{n}_i)$ for atom i with its environment \mathbf{n}_i is linearly expanded as

$$V(\mathbf{n}_i) = \sum_\alpha \xi_\alpha B_\alpha(\mathbf{n}_i), \quad (7)$$

and the energy of the system is then obtained by

$$E^{\text{MTP}} = \sum_i V(\mathbf{n}_i). \quad (8)$$

In practice, the number of basis functions is restricted by a degree-like measure, the maximum level lev_{max} , and, further, atomic interactions beyond a cutoff radius R_{cut} are neglected. To maintain high accuracy at a computationally reasonable number of hyperparameters, a level of $\text{lev}_{\text{max}} = 12$ and a cutoff radius of $R_{\text{cut}} = 5 \text{ \AA}$ were chosen. The weights of the energy and force contributions in the calculation of the loss function were set equal to 1.0, 0.01 \AA^2 , respectively, while stresses were not considered for training.

Ab initio molecular dynamics (AIMD) entering the MTP fitting dataset was performed for all investigated structures at six different volumes at 1600 K. The configurations from the AIMD for each structure served as a preliminary information for training the MTP in the corresponding AL loop.

An AL-loop includes four steps: 1) get/train an MTP; 2) perform classic MD simulations with this MTP to select new configurations; 3) perform DFT calculations for selected configurations and 4) go to step 1). (For a detailed introduction see Ref. [30].) Classic MD simulations were run for 10 picoseconds with the Langevin thermostat at a timestep of 1 femtosecond. MD snapshots were evaluated by calculating the extrapolation grade γ_{mv} according to the maxvol algorithm [30, 53]. The threshold to break an MD simulation was set to $\gamma_{\text{mv}}^{\text{break}} = 3.0$ and the selection threshold to $\gamma_{\text{mv}}^{\text{select}} = 1.5$. An AL-loop was finished if no configuration got selected in step 2), meaning that γ_{mv} for all MD snapshots was below 1.5. As an exception, the AL-loop for the surface structures was run until the extrapolation grade was below 3.0. This is sufficient for the surface structures since they are needed only for the free boundary conditions of the shearing simulations and they have negligible influence on the dislocation behavior.

4.2 Density-functional-theory Calculations

The DFT calculations were performed by using VASP [54, 55] with potentials based on the projector augmented wave (PAW) method [56] and within the PBE-GGA approximation [57] to the exchange-correlation functional. A plane wave cutoff energy of 400 eV was used. Regarding the magnetic contribution, which was concluded to have a significant influence on the formation energy of planar defects in particular for the (100)APB [35], spin-polarization was considered in all the DFT calculations. An MTP trained with a spin-unpolarized dataset was tested and the related discussion is provided in the Supplementary Material (Section ??).

4.3 Free Energy Calculations

The Gibbs energy $G(T)$ was obtained via the Legendre transformation of the Helmholtz free energy $F(T)$, which was computed according to

$$F(T) = E_{0\text{K}} + F^{\text{qh}}(T) + F^{\text{ah}}(T), \quad (9)$$

with the total energy at zero-Kelvin E_{0K} , the quasiharmonic contribution $F^{qh}(T)$ and the anharmonic contribution $F^{ah}(T)$. While F^{qh} was calculated by using the finite displacement method (pre- and post-processing performed with Phonopy [58]), F^{ah} was obtained by using thermodynamic integration from the quasiharmonic reference to the full vibrational state,

$$F^{ah} = \int_0^1 d\lambda \langle E^{\text{vib}} - E^{\text{qh}} \rangle_\lambda, \quad (10)$$

with λ the coupling factor between the full vibrational state with energy E^{vib} and the qh-reference with energy E^{qh} .

The Gibbs formation energy of the planar defects was then obtained as

$$\Delta G_{\text{form}}(T) = \frac{G_{\text{defect}}(T) - G_{\text{bulk}}(T)}{A_{\text{defect}}(T)}, \quad (11)$$

with the Gibbs energies G_{defect} and G_{bulk} of the planar defect and bulk supercell, respectively, and with the area of the planar defect A_{defect} .

4.4 Molecular Dynamics Simulations

ATOMSK [59] was used to generate the initial dislocation configuration according to dislocation theory [60]. Specifically, two $1/2 \langle 1\bar{1}0 \rangle$ screw superpartials were inserted into the model, bound with a (111)APB region, as shown in Figure ??(a). During relaxation, each superpartial dissociated into two Shockley partials, generating a CSF ribbon in between. The dislocation model was made of 1.5 million atoms with dimensions of 20.3 nm, 35.1 nm and 24.8 nm along the x , y and z -axis, respectively. The dislocation line as well as the Burger's vector were placed parallel to the x -axis. Periodic boundary conditions were applied along the x - and y -direction while the boundary conditions along the z -direction were shrink-wrapped.

MTP MD simulations were performed with LAMMPS [61]. To generate an incomplete KWL, the model was first equilibrated at a higher temperature, e.g., 1000 K, to ensure the activation of the cross-slip process within a reasonable simulation time frame. An incomplete KWL with a cross-slip distance of $w = 2\delta$ was selected, quenched to 400 K, and then fully equilibrated at zero pressure. Before the shearing simulations, three statistical samples initiated with different velocities were heated up to the target temperatures in 10 ps and then fully equilibrated for 20 ps. All the MD simulations were performed at a timestep of 0.001 ps.

For the shearing simulations, atoms located within a thickness of 9 atomic planes (≈ 1.9 nm) on the top and bottom of the box were selected to apply the shear (brown regions in Figure ??(a)). These atoms were treated with flexible boundary conditions to avoid spurious forces on the dislocation [62]. The shearing direction was set along the x -axis (parallel to the Burger's vector), such that the core of the dislocation was moving along the y -axis.

The shearing simulations to unlock the incomplete KWL were performed at a set of strain rates $\dot{\gamma} = 1 \times 10^{-5}$, 5×10^{-6} , 2×10^{-6} ps $^{-1}$ and temperatures $T = 650, 700, 800, 850, 900, 950, 1000, 1050, 1100$ K. Test simulations were also performed with $\dot{\gamma}$ of 1×10^{-6} ps $^{-1}$. For each temperature, samples were pre-sheared with $\dot{\gamma} = 1 \times 10^{-4}$ ps $^{-1}$ to a pre-strain γ_0 . Then the production calculations were restarted by continuing shearing from the point of γ_0 with the same atomic state, e.g., atomic positions, velocities and forces. The pre-strain γ_0 was selected such that there was enough time (more than 100 ps) for equilibration before the occurrence of the first cross-slip, e.g., $\gamma_0 = 0.5\%$ for simulations with $\dot{\gamma} = 1 \times 10^{-5}$, 5×10^{-6} ps $^{-1}$. A larger γ_0 was used in the shearing simulations with $\dot{\gamma} = 2 \times 10^{-6}$ ps $^{-1}$, to make sure that unlocking is possible within a reasonable computational time (10 ns). Such a treatment does not only increase the efficiency of the calculations, but also maintains the desired core structure (as illustrated in Figure ??(c)) for high temperature simulations, e.g., at 1000 K. Note that utilizing a high accuracy MTP and performing shearing at a rate of 2×10^{-6} ps $^{-1}$ (or even slower at 1×10^{-6} ps $^{-1}$) for models containing more than one million atoms touches the limits of typical computational resources.

Acknowledgements

The authors acknowledge fruitful discussions with P. Binkele, N. Zotov, K. Gubaev and P. Kumar. This work has been funded by the Deutsche Forschungsgemeinschaft (DFG, German Research Foundation) under the Germany's Excellence Strategy - EXC 2075 – 390740016. We acknowledge the support by the Stuttgart Center for Simulation Science (SimTech) and the funding from the European Research Council (ERC) under the European Unions Horizon 2020 research and innovation programme (Grant Agreement No. 865855). We also acknowledge the support by the state of Baden-Württemberg through bwHPC and the German Research Foundation (DFG) through grant no INST 40/575-1 FUGG (JUSTUS 2 cluster). The shear simulations were performed on the national supercomputer Hawk at the High Performance Computing Center Stuttgart (HLRS) under the grant number H-Embrittlement/44239.

References

- [1] T. Pollock and S. Tin. Nickel-based superalloys for advanced turbine engines: chemistry, microstructure and properties. *Journal of propulsion and power*, 22(2):361–374, 2006. doi: [10.2514/1.18239](https://doi.org/10.2514/1.18239).
- [2] H. Long, S. Mao, Y. Liu, Z. Zhang, and X. Han. Microstructural and compositional design of Ni-based single crystalline superalloys — A review. *Journal of Alloys and Compounds*, 743:203–220, 2018. doi: [10.1016/j.jallcom.2018.01.224](https://doi.org/10.1016/j.jallcom.2018.01.224).
- [3] R. C. Reed. *The superalloys: fundamentals and applications*. Cambridge university press, 2008.
- [4] D. Golberg, M. Demura, and T. Hirano. Effect of Al-rich off-stoichiometry on the yield stress of binary Ni₃Al single crystals. *Acta materialia*, 46(8):2695–2703, 1998. doi: [10.1016/S1359-6454\(97\)00476-X](https://doi.org/10.1016/S1359-6454(97)00476-X).
- [5] S. Takeuchi and E. Kuramoto. Temperature and orientation dependence of the yield stress in Ni₃Ga single crystals. *Acta metallurgica*, 21(4):415–425, 1973. doi: [10.1016/0001-6160\(73\)90198-3](https://doi.org/10.1016/0001-6160(73)90198-3).
- [6] Y. M. Wang-Koh. Understanding the yield behaviour of L1₂-ordered alloys. *Materials Science and Technology*, 33(8):934–943, 2017. doi: [10.1080/02670836.2016.1215961](https://doi.org/10.1080/02670836.2016.1215961).
- [7] Y. Eggeler, K. Vamsi, and T. Pollock. Precipitate shearing, fault energies, and solute segregation to planar faults in Ni-, CoNi-, and Co-base superalloys. *Annual Review of Materials Research*, 51:209–240, 2021. doi: [10.1146/annurev-matsci-102419-011433](https://doi.org/10.1146/annurev-matsci-102419-011433).
- [8] A. Suzuki, H. Inui, and T. Pollock. L1₂-strengthened cobalt-base superalloys. *Annual Review of Materials Research*, 45:345–368, 2015. doi: [10.1146/annurev-matsci-070214-021043](https://doi.org/10.1146/annurev-matsci-070214-021043).
- [9] Z. Chen, K. Kishida, H. Inui, M. Heilmaier, U. Glatzel, and G. Eggeler. Improving the intermediate- and high-temperature strength of L1₂-Co₃ (Al, W) by Ni and Ta additions. *Acta Materialia*, 238:118224, 2022. doi: [10.1016/j.actamat.2022.118224](https://doi.org/10.1016/j.actamat.2022.118224).
- [10] B. X. Cao, H. J. Kong, Z. Y. Ding, S. W. Wu, J. H. Luan, Z. B. Jiao, J. Lu, C. T. Liu, and T. Yang. A novel L1₂-strengthened multicomponent Co-rich high-entropy alloy with both high γ' -solvus temperature and superior high-temperature strength. *Scripta Materialia*, 199:113826, 2021. doi: [10.1103/PhysRevB.50.17953](https://doi.org/10.1103/PhysRevB.50.17953).
- [11] T. Yang, Y. Zhao, W. Liu, J. Kai, and C. Liu. L1₂-strengthened high-entropy alloys for advanced structural applications. *Journal of Materials Research*, 33(19):2983–2997, 2018. doi: [10.1557/jmr.2018.186](https://doi.org/10.1557/jmr.2018.186).
- [12] P. Veyssi re, J. Douin, and P. Beauchamp. On the presence of super lattice intrinsic stacking faults in plastically deformed Ni₃Al. *Philosophical Magazine A*, 51(3):469–483, 1985. doi: [10.1080/01418618508237567](https://doi.org/10.1080/01418618508237567).

- [13] Y. Q. Sun and P. M. Hazzledine. A TEM weak-beam study of dislocations in γ' in a deformed Ni-based superalloy. *Philosophical Magazine A*, 58(4):603–617, 1988. doi: [10.1080/01418618808209940](https://doi.org/10.1080/01418618808209940).
- [14] G. Molenat and D. Caillard. Dislocation mechanisms in Ni₃Al at room temperature. *In situ* straining experiments in TEM. *Philosophical Magazine A*, 64(6):1291–1317, 1991. doi: [10.1080/01418619108225350](https://doi.org/10.1080/01418619108225350).
- [15] C. Coupeau, J. Michel, J. Bonneville, and M. Drouet. An atomic-scale insight into Ni₃Al slip traces. *Materialia*, 9:100563, 2020. doi: [10.1016/j.mtla.2019.100563](https://doi.org/10.1016/j.mtla.2019.100563).
- [16] V. Paidar, D. P. Pope, and V. Vitek. A theory of the anomalous yield behavior in L1₂ ordered alloys. *Acta Metallurgica*, 32(3):435–448, 1984. doi: [10.1016/0001-6160\(84\)90117-2](https://doi.org/10.1016/0001-6160(84)90117-2).
- [17] M. H. Yoo. On the theory of anomalous yield behavior of Ni₃Al—Effect of elastic anisotropy. *Scr. Metall.:(United States)*, 20(6), 1986. doi: [10.1016/0036-9748\(86\)90466-7](https://doi.org/10.1016/0036-9748(86)90466-7).
- [18] P. B. Hirsch. A new theory of the anomalous yield stress in L1₂ alloys. *Philosophical Magazine A*, 65(3):569–612, 1992. doi: [10.1080/01418619208201539](https://doi.org/10.1080/01418619208201539).
- [19] D. Caillard and V. Paidar. A model for the anomalous mechanical properties of nickel-base L1₂ ordered alloys—I. Dislocations dynamics. *Acta materialia*, 44(7):2759–2771, 1996. doi: [10.1016/1359-6454\(95\)00388-6](https://doi.org/10.1016/1359-6454(95)00388-6).
- [20] T. Kruml, E. Conforto, B. Lo. Piccolo, D. Caillard, and J. L. Martin. From dislocation cores to strength and work-hardening: a study of binary Ni₃Al. *Acta materialia*, 50(20):5091–5101, 2002. doi: [10.1016/S1359-6454\(02\)00364-6](https://doi.org/10.1016/S1359-6454(02)00364-6).
- [21] Y. S. Choi, D. M. Dimiduk, M. D. Uchic, and T. A. Parthasarathy. Modelling plasticity of Ni₃Al-based L1₂ intermetallic single crystals. I. Anomalous temperature dependence of the flow behaviour. *Philosophical Magazine*, 87(12):1939–1965, 2007. doi: [10.1080/14786430601169782](https://doi.org/10.1080/14786430601169782).
- [22] M. Demura, D. Golberg, and T. Hirano. An athermal deformation model of the yield stress anomaly in Ni₃Al. *Intermetallics*, 15(10):1322–1331, 2007. doi: [10.1016/j.intermet.2007.04.007](https://doi.org/10.1016/j.intermet.2007.04.007).
- [23] M. H. Yoo, M. S. Daw, and M. I. Baskes. Atomistic simulation of superdislocation dissociation in Ni₃Al. *Atomistic Simulation of Materials: Beyond Pair Potentials*, pages 401–410, 1989. doi: [10.1007/978-1-4684-5703-2](https://doi.org/10.1007/978-1-4684-5703-2).
- [24] M. Wen and D. L. Lin. Effect of elastic center on dislocation core structure in ni3al. *Acta materialia*, 45(3):1005–1008, 1997. doi: [10.1016/S1359-6454\(96\)00229-7](https://doi.org/10.1016/S1359-6454(96)00229-7).
- [25] T. Parthasarathy and D. Dimiduk. Atomistic simulations of the structure and stability of “PPV” locks in an L1₂ compound. *Acta materialia*, 44(6):2237–2247, 1996. doi: [10.1016/1359-6454\(95\)00362-2](https://doi.org/10.1016/1359-6454(95)00362-2).
- [26] A. H. W. Ngan, M. Wen, and C. H. Woo. Atomistic simulations of Paidar–Pope–Vitek lock formation in Ni₃Al. *Computational materials science*, 29(3):259–269, 2004. doi: [10.1016/j.commatsci.2003.10.003](https://doi.org/10.1016/j.commatsci.2003.10.003).
- [27] S. Rao, D. Dimiduk, T. Parthasarathy, M. Uchic, and C. Woodward. Atomistic simulations of intersection cross-slip nucleation in L1₂ Ni₃Al. *Scripta Materialia*, 66(6):410–413, 2012. doi: [10.1016/j.scriptamat.2011.12.002](https://doi.org/10.1016/j.scriptamat.2011.12.002).
- [28] M. Wakeda, T. Osada, and T. Ohmura. Atomistic analysis of temperature-dependent dislocation dynamics in Ni₃Al-based intermetallic alloys. *Materials Today Communications*, 37:106987, 2023. doi: [10.1016/j.mtcomm.2023.106987](https://doi.org/10.1016/j.mtcomm.2023.106987).
- [29] A. V. Shapeev. Moment tensor potentials: A class of systematically improvable interatomic potentials. *Multiscale Modeling & Simulation*, 14(3):1153–1173, 2016. doi: [10.1137/15M1054183](https://doi.org/10.1137/15M1054183).

- [30] K. Gubaev, E. V. Podryabinkin, G. L. W. Hart, and A. V. Shapeev. Accelerating high-throughput searches for new alloys with active learning of interatomic potentials. *Computational Materials Science*, 156:148–156, 2019. doi: [10.1016/j.commatsci.2018.09.031](https://doi.org/10.1016/j.commatsci.2018.09.031).
- [31] T. Lee, J. Qi, C. A. Gadre, H. Huyan, S. T. Ko, Y. X. Zuo, C. J. Du, J. Li, T. Aoki, R. Q. Wu, et al. Atomic-scale origin of the low grain-boundary resistance in perovskite solid electrolyte $\text{Li}_{0.375}\text{Sr}_{0.4375}\text{Ta}_{0.75}\text{Zr}_{0.25}\text{O}_3$. *Nature Communications*, 14(1):1940, 2023. doi: [10.1038/s41467-023-37115-6](https://doi.org/10.1038/s41467-023-37115-6).
- [32] S. Yin, Y. Zuo, A. Abu-Odeh, H. Zheng, X. G. Li, J. Ding, S. P. Ong, M. Asta, and R. O. Ritchie. Atomistic simulations of dislocation mobility in refractory high-entropy alloys and the effect of chemical short-range order. *Nature communications*, 12(1):4873, 2021. doi: [10.1038/s41467-021-25134-0](https://doi.org/10.1038/s41467-021-25134-0).
- [33] L. Erhard, J. Rohrer, K. Albe, and V. Deringer. Modelling atomic and nanoscale structure in the silicon–oxygen system through active machine learning. *Nature Communications*, 15(1):1927, 2024. doi: [10.1038/s41467-024-45840-9](https://doi.org/10.1038/s41467-024-45840-9).
- [34] L. Mismetti and M. Hodapp. Automated atomistic simulations of dissociated dislocations with ab initio accuracy. *Physical Review B*, 109(9):094120, 2024. doi: [10.1103/PhysRevB.109.094120](https://doi.org/10.1103/PhysRevB.109.094120).
- [35] X. Xu, X. Zhang, A. Ruban, S. Schmauder, and B. Grabowski. Strong impact of spin fluctuations on the antiphase boundaries of weak itinerant ferromagnetic Ni_3Al . *Acta Materialia*, 255:118986, 2023. doi: [10.1016/j.actamat.2023.118986](https://doi.org/10.1016/j.actamat.2023.118986).
- [36] X. Xu, X. Zhang, A. Ruban, S. Schmauder, and B. Grabowski. Accurate complex-stacking-fault gibbs energy in Ni_3Al at high temperatures. *Scripta Materialia*, 242:115934, 2024. doi: [10.1016/j.scriptamat.2023.115934](https://doi.org/10.1016/j.scriptamat.2023.115934).
- [37] Y. Mishin. Atomistic modeling of the γ and γ' -phases of the Ni–Al system. *Acta Materialia*, 52(6):1451–1467, 2004. doi: [10.1016/j.actamat.2003.11.026](https://doi.org/10.1016/j.actamat.2003.11.026).
- [38] J. P. Du, C. Y. Wang, and T. Yu. Construction and application of multi-element EAM potential (Ni–Al–Re) in γ/γ' Ni-based single crystal superalloys. *Modelling and Simulation in Materials Science and Engineering*, 21(1):015007, 2012. doi: [10.1088/0965-0393/21/1/015007](https://doi.org/10.1088/0965-0393/21/1/015007).
- [39] A. Stukowski and K. Albe. Extracting dislocations and non-dislocation crystal defects from atomistic simulation data. *Modelling and Simulation in Materials Science and Engineering*, 18(8):085001, 2010. Website: [10.1088/0965-0393/18/8/085001](https://doi.org/10.1088/0965-0393/18/8/085001).
- [40] M. H. Yoo. Stability of superdislocations and shear faults in L_{12} ordered alloys. *Acta Metallurgica*, 35(7):1559–1569, 1987. doi: [10.1016/0001-6160\(87\)90102-7](https://doi.org/10.1016/0001-6160(87)90102-7).
- [41] U. Kocks, A. Argon, and M. Ashby. *Thermodynamics and kinetics of slip*. 1975.
- [42] S. Nemat-Nasser and W. Guo. Flow stress of commercially pure niobium over a broad range of temperatures and strain rates. *Materials Science and Engineering: A*, 284(1-2):202–210, 2000. doi: [10.1016/S0921-5093\(00\)00740-1](https://doi.org/10.1016/S0921-5093(00)00740-1).
- [43] N. Zotov and B. Grabowski. Molecular dynamics simulations of screw dislocation mobility in bcc Nb. *Modelling and Simulation in Materials Science and Engineering*, 29(8):085007, 2021. doi: [10.1088/1361-651X/ac2b02](https://doi.org/10.1088/1361-651X/ac2b02).
- [44] J. Li. The mechanics and physics of defect nucleation. *MRS bulletin*, 32(2):151–159, 2007. doi: [10.1557/mrs2007.48](https://doi.org/10.1557/mrs2007.48).
- [45] J. Bonneville, J. L. Martin, P. Spätig, B. Viguier, and B. Matterstock. Mechanical properties of binary Ni_3Al single crystals. *MRS Online Proceedings Library (OPL)*, 460, 1996. doi: [10.1557/PROC-460-419](https://doi.org/10.1557/PROC-460-419).

- [46] H. P. Karnthaler, E. Th. Mühlbacher, and C. Rentenberger. The influence of the fault energies on the anomalous mechanical behaviour of Ni₃Al alloys. *Acta Materialia*, 44(2):547–560, 1996. doi: [10.1016/1359-6454\(95\)00191-3](https://doi.org/10.1016/1359-6454(95)00191-3).
- [47] C. Rentenberger and H. Karnthaler. On the origin of work softening of Ni₃Al deformed along [001] above the peak temperature. *Materials Science and Engineering: A*, 319:347–351, 2001. doi: [10.1016/S0921-5093\(01\)01022-X](https://doi.org/10.1016/S0921-5093(01)01022-X).
- [48] T. Kruml, J. L. Martin, B. Viguier, J. Bonneville, and P. Spätig. Deformation microstructures in Ni₃(Al, Hf). *Materials Science and Engineering: A*, 239:174–179, 1997. doi: [10.1016/S0921-5093\(97\)00578-9](https://doi.org/10.1016/S0921-5093(97)00578-9).
- [49] E. Conforto, G. Molénat, and D. Caillard. Comparison of Ni-based alloys with extreme values of antiphase boundary energies: dislocation mechanisms and mechanical properties. *Philosophical Magazine*, 85(2-3):117–137, 2005. doi: [10.1080/14786430412331315626](https://doi.org/10.1080/14786430412331315626).
- [50] X. X. Yu and C. Y. Wang. Effect of alloying element on dislocation cross-slip in γ' -Ni₃Al: a first-principles study. *Philosophical Magazine*, 92(32):4028–4039, 2012. doi: [10.1080/14786435.2012.700419](https://doi.org/10.1080/14786435.2012.700419).
- [51] K. Vamsi and S. Karthikeyan. Yield anomaly in L1₂ Co₃Al_xW_{1-x} vis-à-vis Ni₃Al. *Scripta Materialia*, 130:269–273, 2017. doi: [10.1016/j.scriptamat.2016.11.039](https://doi.org/10.1016/j.scriptamat.2016.11.039).
- [52] K. Vamsi and S. Karthikeyan. High-throughput estimation of planar fault energies in A₃B compounds with L1₂ structure. *Acta Materialia*, 145:532–542, 2018. doi: [10.1016/j.actamat.2017.10.029](https://doi.org/10.1016/j.actamat.2017.10.029).
- [53] I. S. Novikov, K. Gubaev, E. V. Podryabinkin, and A. V. Shapeev. The mlip package: moment tensor potentials with MPI and active learning. *Machine Learning: Science and Technology*, 2(2):025002, 2020. Website: [10.1088/2632-2153/abc9fe](https://doi.org/10.1088/2632-2153/abc9fe).
- [54] G. Kresse and J. Hafner. Ab initio molecular dynamics for liquid metals. *Physical Review B*, 47:558–561, Jan 1993. doi: [10.1103/PhysRevB.47.558](https://doi.org/10.1103/PhysRevB.47.558).
- [55] G. Kresse and J. Hafner. Ab initio molecular-dynamics simulation of the liquid-metal–amorphous-semiconductor transition in germanium. *Physical Review B*, 49:14251–14269, May 1994. doi: [10.1103/PhysRevB.49.14251](https://doi.org/10.1103/PhysRevB.49.14251).
- [56] Peter E Blöchl. Projector augmented-wave method. *Physical review B*, 50(24):17953, 1994. doi: [10.1103/PhysRevB.50.17953](https://doi.org/10.1103/PhysRevB.50.17953).
- [57] J. P. Perdew, K. Burke, and M. Ernzerhof. Generalized gradient approximation made simple. *Physical Review Letters*, 77:3865–3868, Oct 1996. doi: [10.1103/PhysRevLett.77.3865](https://doi.org/10.1103/PhysRevLett.77.3865).
- [58] A. Togo and I. Tanaka. First principles phonon calculations in materials science. *Scripta Materialia*, 108:1–5, 2015. doi: [10.1016/j.scriptamat.2015.07.021](https://doi.org/10.1016/j.scriptamat.2015.07.021).
- [59] P. Hirel. AtomsK: A tool for manipulating and converting atomic data files. *Computer Physics Communications*, 197:212–219, 2015. Website: [10.1016/j.cpc.2015.07.012](https://doi.org/10.1016/j.cpc.2015.07.012).
- [60] P. M. Anderson, J. P. Hirth, and J. Lothe. *Theory of dislocations*. Cambridge University Press, 2017.
- [61] A. P. Thompson, H. M. Aktulga, R. Berger, D. S. Bolintineanu, M. Brown, P. Crozier, P. in’t Veld, A. Kohlmeyer, S. Moore, T. Nguyen, et al. LAMMPS—a flexible simulation tool for particle-based materials modeling at the atomic, meso, and continuum scales. *Computer Physics Communications*, 271:108171, 2022. Website: [10.1016/j.cpc.2021.108171](https://doi.org/10.1016/j.cpc.2021.108171).
- [62] D. Rodney. Activation enthalpy for kink-pair nucleation on dislocations: Comparison between static and dynamic atomic-scale simulations. *Physical Review B*, 76(14):144108, 2007. doi: [10.1103/PhysRevB.76.144108](https://doi.org/10.1103/PhysRevB.76.144108).

Supplementary Information to “Origin of the yield stress anomaly in L1₂ intermetallics unveiled with physically-informed machine-learning potentials”

Xiang Xu^{1,2,*}, Xi Zhang^{1,*}, Erik Bitzek³, Siegfried Schmauder², and Blazej Grabowski¹

¹*Institute for Materials Science, University of Stuttgart, Pfaffenwaldring 55, 70569 Stuttgart, Germany*

²*Institute for Materials Testing, Materials Science and Strength of Materials, University of Stuttgart, Pfaffenwaldring 32, 70569 Stuttgart, Germany*

³*Computational Materials Design, Max Planck Institute for Sustainable Materials, Max-Planck-Straße 1, 40237 Düsseldorf, Germany.*

*Emails: xiang.xu@imw.uni-stuttgart.de; xi.zhang@imw.uni-stuttgart.de

S1 Kear-Wilmsdorf locks

Figure S1 shows schematically the structural evolution of a screw superdislocation in Ni₃Al, i.e., the formation of a Kear-Wilmsdorf lock (KWL). The involved planar defects are the antiphase boundaries (APB) on the (100) and (111) planes and the complex stacking fault (CSF). In (b) a pair of Shockley partials constricts into one superpartial, ready for cross-slipping. Depending on the cross-slip distance w , either an incomplete KWL made of a (100)APB, (111)APB and CSF forms as shown in (c), or a complete KWL develops, for which the superdislocation dissociates into two superpartials only spanning on a (100) plane (no (111)APB) as shown in (d).

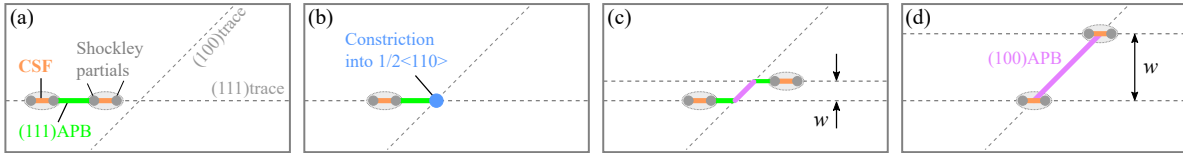


Figure S1: Schematic diagram of the formation of a KWL. (a) The core structure of a glissile superdislocation. (b) Constriction of the leading superpartial. (c) An incomplete KWL and (d) a complete KWL.

S2 Atomistic model

The atomistic model of the core configuration of a screw superdislocation is shown in Figure S2. The superdislocation dissociates according to

$$[\bar{1}10] \rightarrow \underbrace{\frac{1}{2}[\bar{1}10]}_A + \text{APB} + \underbrace{\frac{1}{2}[\bar{1}10]}_B \quad (\text{S1})$$

$$\rightarrow \underbrace{\frac{1}{6}[\bar{1}2\bar{1}] + \text{CSF} + \frac{1}{6}[\bar{2}11]}_{a_1 \text{ and } a_2 \text{ on a (111) plane}} + \text{APB} + \underbrace{\frac{1}{6}[\bar{1}2\bar{1}] + \text{CSF} + \frac{1}{6}[\bar{2}11]}_{b_1 \text{ and } b_2 \text{ on a (111) plane}} \quad (\text{S2})$$

$$\rightarrow \underbrace{\frac{1}{6}[\bar{1}2\bar{1}] + \text{CSF} + \frac{1}{6}[\bar{2}11]}_{a_1 \text{ and } a_2 \text{ on a (111) plane}} + \text{APB} + \underbrace{\frac{1}{6}[\bar{2}1\bar{1}] + \text{CSF} + \frac{1}{6}[\bar{1}21]}_{b_1 \text{ and } b_2 \text{ on a (111) plane}} \quad (\text{S3})$$

Equation (S1) expresses the dissociation of the superdislocation into two superpartials (blue lines labelled A and B in Figure S2(a)). Each of the superpartials further dissociates into two Shockley partials (green lines a_1 , a_2 , b_1 and b_2 in Figure S2(b)) according to Equation (S2) after relaxation. The green and red region represent the (111)APB and the CSF, respectively. The core configuration described by Equation (S3) is the intermediate state when superpartials cross-slip onto a ($\bar{1}\bar{1}1$) plane (equivalent to the (111) plane).

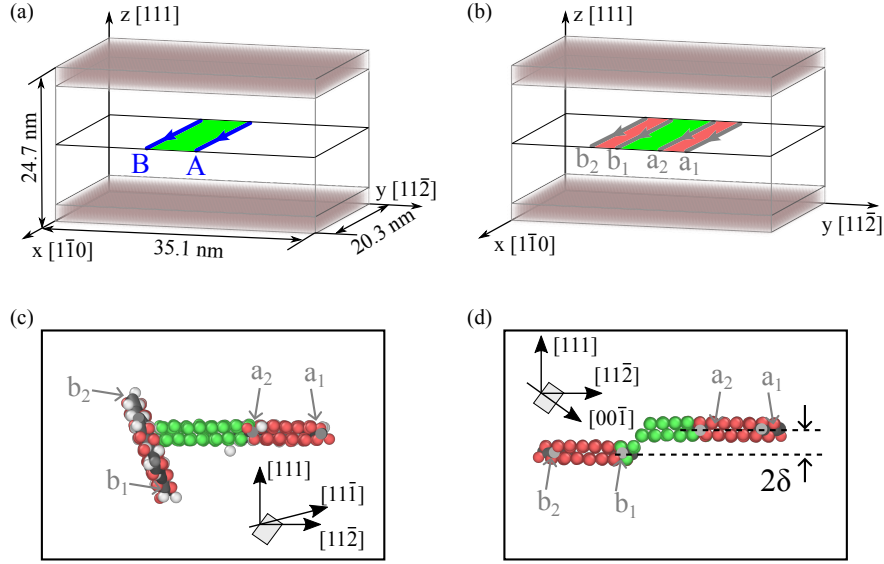


Figure S2: Model of the $\langle \bar{1}10 \rangle$ screw superdislocation in Ni₃Al. (a) Initial core structure with two superpartials bound with a (111)APB. (b) Core structure after relaxation. Brown regions on the top and bottom of the simulation box are used to perform shearing. The arrows represent the dislocation line directions. (c) and (d) Atomistic models for core structures of two incomplete KWLs with a cross-slip distance of 0.5δ and 2δ , respectively. (c) corresponds to the core configuration described by Equation (S3) and (d) to Equation (S2). Structural analysis is performed by using OVITO [1] with the DXA algorithm [2]. Only atoms in the dislocation core structure are shown. Green and red atoms represent the atoms in the APB and CSF regions.

When equilibrating without external loading, the leading and trailing superpartial have the same probability to cross-slip onto the (100) plane, which is implied by Figure S3.

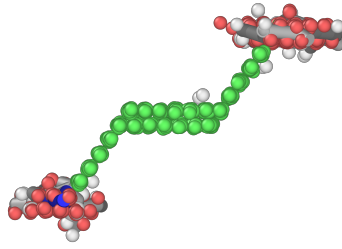


Figure S3: Core structure of the $\langle \bar{1}10 \rangle$ screw superdislocation in Ni₃Al after equilibration without external loading at 1100 K for 1 ns. Atom colors have the same meaning as in Figure S2.

S3 Physically-informed active learning

Table S1 records training set sizes and training errors of each active-learning (AL) step for a Moment Tensor Potential (MTP). The length of the AL-steps after the bulk geometry AL-step are significantly reduced (less configurations selected from AL and less learning iterations). Importantly, when adding a new structure, the training errors change only slightly, indicating the stability of the input MTP potential from the previous step.

Table S1: Training set sizes and fitting errors (RMSE: root mean square error) during the physically-informed AL scheme.

Geometries	# of selected configurations		RMSE		# of learning steps
	from AIMD	from AL	Energy (meV/atom)	Force (eV/Å)	
bulk	180	218	0.66	0.047	7
(100)APB	45	76	0.93	0.050	3
(111)APB	167	87	1.04	0.049	6
CSF	45	21	1.14	0.050	2
SISF	39	6	1.15	0.049	1
Ni-vacancy	45	42	1.16	0.050	2
Al-vacancy	45	44	1.38	0.050	2
(100)surface [†]	45	57	1.59	0.056	2
(111)surface [*]	0	0	1.59	0.056	0

[†] Since the dislocation activity does not depend directly on the surface atoms, the criterion for this AL-step is set as $\theta_{\text{select}} < 3$.

^{*} The MTP trained with the (100)surface configurations can likewise well describe the (111)surface.

S4 Prediction of elastic constants

The elastic constants of Ni₃Al are provided in Table S2, including results from experimental and DFT studies. The anisotropic factor A , also known as the Zener factor, is [3]

$$A = \frac{2C_{44}}{C_{11} - C_{12}}. \quad (\text{S4})$$

The shear moduli on the (111) plane along $[11\bar{2}]$ and $[\bar{1}\bar{1}0]$ direction are [4]

$$\mu_{112} = \frac{3C_{44}(C_{11} - C_{12})}{C_{11} - C_{12} + 4C_{44}}, \quad (\text{S5})$$

$$\mu_{110} = \frac{3C_{44}(C_{11} - C_{12})}{2(C_{11} - C_{12} + C_{44})}. \quad (\text{S6})$$

In general, C_{11} and C_{12} from the utilized MTP agree well with those from other studies, while C_{44} and A are underestimated. Further, B , μ , μ_{112} and μ_{110} also show good agreement with previous studies.

Table S2: Elastic properties at 0 K of Ni₃Al in units of GPa (A is dimensionless). B , μ , and Y are the bulk modulus, the shear modulus and the Young’s modulus, respectively. Data from literature are Prikhodko1999 at 300 K [5], Zhao2015-DFT [6] and Luan2018-DFT [7]. EAM results: Mishin2004 [8], Du2012 [9].

	C_{11}	C_{12}	C_{44}	B	Y	A	μ	μ_{112}	μ_{110}
MTP (this work)	231.8	150.3	106.6	177.5	191.3	2.62	72.5	51.28	69.28
Prikhodko1999-exp.	224.5	148.6	124.4	173.9	203.1	3.28	77.8	49.39	70.71
Zhao2015-DFT	232.7	154.5	123.0	180.6	204.0	3.14	77.8	50.61	71.82
Mishin2004	236.0	154.3	127.1	181.5	210.9	3.11	80.7	52.95	74.60
Du2012	242.6	149.3	130.3	180.4	223.4	2.79	86.4	59.35	81.55

S5 Atomic extrapolation grades

The atomic extrapolation grades θ_{local} are calculated by using the package MLIP-3 [10] with an extra function for evaluating atomic neighborhoods. The functional form of the MTP remains the same as in MLIP-2 [11] which has been mainly utilized in the present work. The local grades for the reference KWL structure (Figure S4(a)) were calculated with different MTPs and are shown in Figure S4(b)-(d). “MTP-bulk” in (b), “MTP-100APB” in (c), and “MTP-111APB” in (d) represent MTPs trained with bulk configurations, bulk+(100)APB configurations, and bulk+(100)APB+(111)APB configurations, respectively, following the scheme shown in Figure 1 in the main text. For the relevant discussion on Figure S4, please see Section 2.1 in the main text.

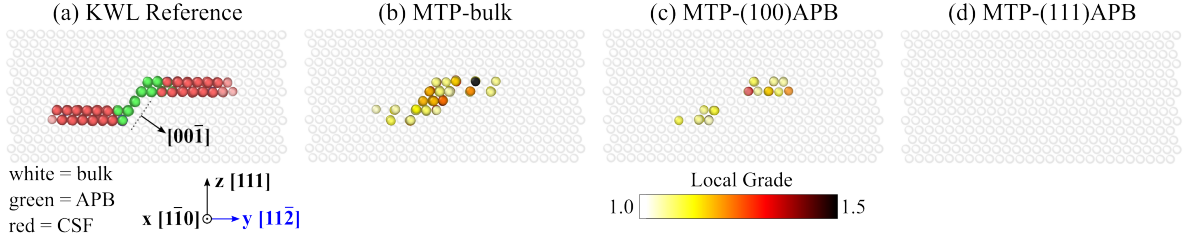


Figure S4: (a) Atomic environment around a KWL. (b) - (d) Atomic extrapolation grades around the selected KWL environment.

S6 Performance of MTP

An alternative MTP was trained with a spin-unpolarized DFT dataset following the proposed physically informed active-learning scheme, named as “MTP-NM” to distinguish it from the “MTP” based on the spin-polarized DFT dataset. Its predictive performance is displayed in Figure S5 and S6. From Figure S5, there is only a slight difference between the thermal properties of the MTPs trained with the spin-polarized and nonpolarized DFT dataset. However, the Gibbs energies of the planar defects show significant difference between these MTPs, as plotted in Figure S6. Specifically, the predicted Gibbs formation energies for (100)APB and for (111)APB from “MTP-NM” are smaller than that from “MTP”. This is reasonable because magnetism was reported to strongly influence the formation energy for (100)APB and (111)APB [12], in particular for (100)APB. Overall, the MTP trained with spin-polarized DFT configurations shows a better agreement with the full DFT results.

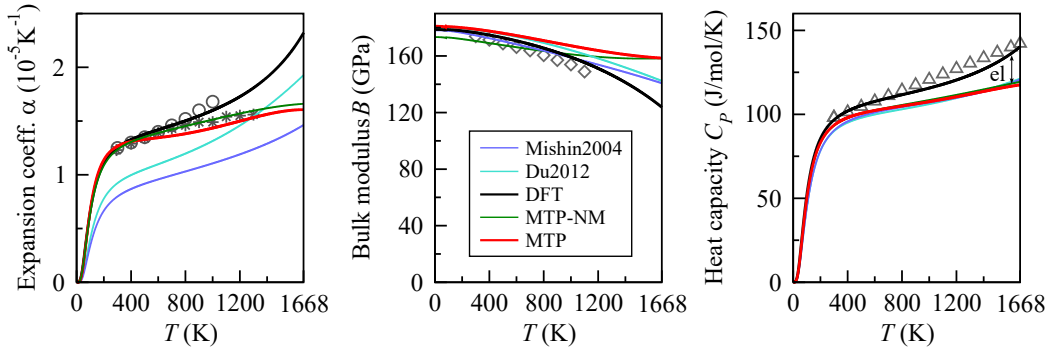


Figure S5: Thermal properties of Ni_3Al . Experimental data: α : circles [13] and stars [14]; B [5]; C_p [15]. EAM results: Mishin2004 [8], Du2012 [9].

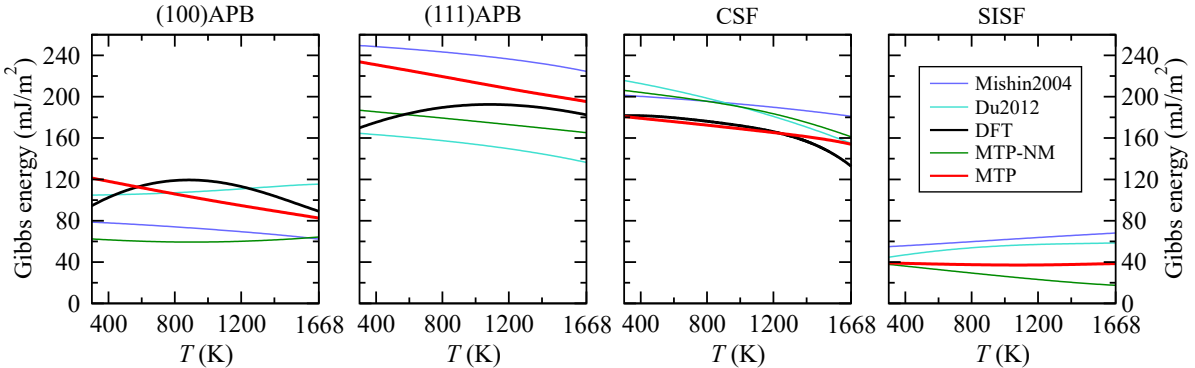


Figure S6: Gibbs energy of planar defects in Ni_3Al . EAM results: Mishin2004 [8], Du2012 [9].

S7 Extrapolation of the phenomenological model

The pre-factor $\dot{\gamma}_0$ corresponds to the ideal plastic shear rate when dislocations are mobile, following Orowan's equation

$$\dot{\gamma}_0 = \rho b v_0, \quad (\text{S7})$$

with the dislocation density ρ , the length of the Burger's vector b and the initial velocity v_0 . For Ni₃Al, the initial dislocation density ρ_m was taken to be $1 \times 10^{12} \text{ m}^{-2}$ [16]. v_0 can be reasonably approximated as the maximum velocity 1500 m/s from MD simulations [17]. Therefore, $\dot{\gamma}_{0,m}$ is $7.575 \times 10^5 \text{ s}^{-1}$ for a $\langle 1\bar{1}0 \rangle$ superdislocation in Ni₃Al with a Burger's vector of 5.05 Å. The order of magnitude is comparable with the typically utilized value of $1 \times 10^7 \text{ s}^{-1}$ in other studies [18, 19]. Setting the strain rate $\dot{\gamma}_m = 2.3 \times 10^{-4} \text{ s}^{-1}$ as in compression tests [20], the model can be extrapolated to the macroscale, by introducing the logarithmic term $\ln(\dot{\gamma}_m/\dot{\gamma}_{0,m})$. A similar treatment has been successfully applied in a previous work [18].

S8 Static analysis based on elastic anisotropy theory

For a free dislocation (without external loading) spanning on the (111) plane (Figure S1(a)), there are internal driving forces that can cause dislocation cross-slip. These internal driving forces come from 1) the difference between the energies of the (100)APB and (111)APB [21] and 2) the elastic anisotropy causing a torque interaction between the two screw superpartials [3], which has the form

$$\tau_{\text{int}}(T) = \frac{1}{b(T)} \left(\frac{\sqrt{3}A}{A+2} \Delta G_{111}(T) - \Delta G_{100}(T) \right). \quad (\text{S8})$$

References

- [1] A. Stukowski. Visualization and analysis of atomistic simulation data with OVITO—the Open Visualization Tool. *Modelling and simulation in materials science and engineering*, 18(1):015012, 2009. doi: [10.1088/0965-0393/18/1/015012](https://doi.org/10.1088/0965-0393/18/1/015012).
- [2] A. Stukowski and K. Albe. Extracting dislocations and non-dislocation crystal defects from atomistic simulation data. *Modelling and Simulation in Materials Science and Engineering*, 18(8):085001, 2010. Website: [10.1088/0965-0393/18/8/085001](https://doi.org/10.1088/0965-0393/18/8/085001).
- [3] M. H. Yoo. On the theory of anomalous yield behavior of Ni₃Al—Effect of elastic anisotropy. *Scr. Metall.:(United States)*, 20(6), 1986. doi: [10.1016/0036-9748\(86\)90466-7](https://doi.org/10.1016/0036-9748(86)90466-7).
- [4] M. Jahnátek, J. Hafner, and M. Krajčí. Shear deformation, ideal strength, and stacking fault formation of fcc metals: A density-functional study of Al and Cu. *Physical Review B*, 79(22):224103, 2009. doi: [10.1103/PhysRevB.79.224103](https://doi.org/10.1103/PhysRevB.79.224103).
- [5] S. V. Prikhodko, H. Yang, A. J. Ardell, J. D. Carnes, and D. G. Isaak. Temperature and composition dependence of the elastic constants of Ni₃Al. *Metallurgical and Materials Transactions A*, 30(9):2403–2408, 1999. doi: [10.1007/s11661-999-0248-9](https://doi.org/10.1007/s11661-999-0248-9).
- [6] W. Y. Zhao, Z. M. Sun, and S. K. Gong. Synergistic effect of co-alloying elements on site preferences and elastic properties of Ni₃Al: A first-principles study. *Intermetallics*, 65:75–80, 2015. doi: [10.1016/j.intermet.2015.06.006](https://doi.org/10.1016/j.intermet.2015.06.006).
- [7] X. Luan, H. Qin, F. Liu, Z. Dai, Y. Yi, and Q. Li. The mechanical properties and elastic anisotropies of cubic Ni₃Al from first principles calculations. *Crystals*, 8(8):307, 2018. doi: [10.3390/cryst8080307](https://doi.org/10.3390/cryst8080307).
- [8] Y. Mishin. Atomistic modeling of the γ and γ' -phases of the Ni–Al system. *Acta Materialia*, 52(6):1451–1467, 2004. doi: [10.1016/j.actamat.2003.11.026](https://doi.org/10.1016/j.actamat.2003.11.026).
- [9] J. P. Du, C. Y. Wang, and T. Yu. Construction and application of multi-element EAM potential (Ni–Al–Re) in γ/γ' Ni-based single crystal superalloys. *Modelling and Simulation in Materials Science and Engineering*, 21(1):015007, 2012. doi: [10.1088/0965-0393/21/1/015007](https://doi.org/10.1088/0965-0393/21/1/015007).
- [10] E. Podryabinkin, K. Garifullin, A. Shapeev, and I. Novikov. MLIP-3: Active learning on atomic environments with Moment Tensor Potentials. *arXiv preprint arXiv:2304.13144*, 2023.

- [11] I. S. Novikov, K. Gubaev, E. V. Podryabinkin, and A. V. Shapeev. The mlip package: moment tensor potentials with MPI and active learning. *Machine Learning: Science and Technology*, 2(2):025002, 2020. Website: [10.1088/2632-2153/abc9fe](https://doi.org/10.1088/2632-2153/abc9fe).
- [12] X. Xu, X. Zhang, A. Ruban, S. Schmauder, and B. Grabowski. Strong impact of spin fluctuations on the antiphase boundaries of weak itinerant ferromagnetic Ni₃Al. *Acta Materialia*, 255:118986, 2023. doi: [10.1016/j.actamat.2023.118986](https://doi.org/10.1016/j.actamat.2023.118986).
- [13] Y. S. Touloukian, R. K. Kirby, R. E. Taylor, and P. D. Desai. *Thermophysical properties of matter - the TPRC data series. Volume 12. Thermal expansion metallic elements and alloys. (Reannouncement)*. Data book, 1975.
- [14] R. K. Williams, R. S. Graves, F. J. Weaver, and D. L. McElroy. Physical properties of Ni₃Al containing 24 and 25 atomic percent aluminum. *MRS Proceedings*, 39:505, 1984. doi: [10.1557/PROC-39-505](https://doi.org/10.1557/PROC-39-505).
- [15] I. Barin and G. Platzki. *Thermochemical Data of Pure Substances*. Wiley, 1995.
- [16] T. Kruml and J. Martin. Dislocation densities and internal stress in Ni₃Al. *Philosophical Magazine*, 93(1-3):50–59, 2013. doi: [10.1080/14786435.2012.706371](https://doi.org/10.1080/14786435.2012.706371).
- [17] M. Wakeda, T. Osada, and T. Ohmura. Atomistic analysis of temperature-dependent dislocation dynamics in Ni₃Al-based intermetallic alloys. *Materials Today Communications*, 37:106987, 2023. doi: [10.1016/j.mtcomm.2023.106987](https://doi.org/10.1016/j.mtcomm.2023.106987).
- [18] Z. Li, Z. Liu, Z. Zhuang, and Y. Cui. Temperature dependent deformation localization in irradiated tungsten. *International Journal of Plasticity*, 146:103077, 2021. doi: [10.1016/j.ijplas.2021.103077](https://doi.org/10.1016/j.ijplas.2021.103077).
- [19] I. Beyerlein and C. Tomé. A dislocation-based constitutive law for pure Zr including temperature effects. *International Journal of Plasticity*, 24(5):867–895, 2008. doi: [10.1016/j.ijplas.2007.07.017](https://doi.org/10.1016/j.ijplas.2007.07.017).
- [20] D. Golberg, M. Demura, and T. Hirano. Effect of Al-rich off-stoichiometry on the yield stress of binary Ni₃Al single crystals. *Acta materialia*, 46(8):2695–2703, 1998. doi: [10.1016/S1359-6454\(97\)00476-X](https://doi.org/10.1016/S1359-6454(97)00476-X).
- [21] V. Paidar, D. P. Pope, and V. Vitek. A theory of the anomalous yield behavior in L1₂ ordered alloys. *Acta Metallurgica*, 32(3):435–448, 1984. doi: [10.1016/0001-6160\(84\)90117-2](https://doi.org/10.1016/0001-6160(84)90117-2).